ARTICLES
https://doi.org/10.1038/s41563-021-01183-0
nature materials

Check for updates

Tandem catalysis with double-shelled hollow spheres

Jiadong Xiao[1,4,8], Kang Cheng[2,8], Xiaobin Xie[3,5], Mengheng Wang[2], Shiyou Xing[1], Yuanshuai Liu[1,6], Thomas Hartman[1], Donglong Fu[1,7], Koen Bossers[1], Marijn A. van Huis[3], Alfons van Blaaderen[3], Ye Wang[2]✉ and Bert M. Weckhuysen[1]✉

Metal–zeolite composites with metal (oxide) and acid sites are promising catalysts for integrating multiple reactions in tandem to produce a wide variety of wanted products without separating or purifying the intermediates. However, the conventional design of such materials often leads to uncontrolled and non-ideal spatial distributions of the metal inside/on the zeolites, limiting their catalytic performance. Here we demonstrate a simple strategy for synthesizing double-shelled, contiguous metal oxide@zeolite hollow spheres (denoted as MO@ZEO DSHSs) with controllable structural parameters and chemical compositions. This involves the self-assembly of zeolite nanocrystals onto the surface of metal ion-containing carbon spheres followed by calcination and zeolite growth steps. The step-by-step formation mechanism of the material is revealed using mainly in situ Raman spectroscopy and X-ray diffraction and ex situ electron microscopy. We demonstrate that it is due to this structure that an Fe_2O_3@H-ZSM-5 DSHSs-showcase catalyst exhibits superior performance compared with various conventionally structured Fe_2O_3-H-ZSM-5 catalysts in gasoline production by the Fischer–Tropsch synthesis. This work is expected to advance the rational synthesis and research of hierarchically hollow, core–shell, multifunctional catalyst materials.

Structural engineering, briefly defined as processing materials into desired, well-defined architectures, bridges the interplay between properties and performance and is the cornerstone of the science and technology of current functional materials[1,2]. A typical and yet important example is the design and synthesis of well-structured and highly performing bi- and multi-functional solid catalysts[3–6], where the performance is largely affected by the structure of each catalytic component, spanning from the atomic scale to the microarchitecture, and by the spatial organization of the different components. Such materials could be very active for tandem catalysis, an effective process intensification strategy for chemical processes by coupling multiple consecutive chemical reactions in a single vessel/catalyst and under similar or identical conditions[7–9]. Metal oxide–zeolite (MO–ZEO) bifunctional catalysts have been frequently explored to mediate tandem reactions, because MO and ZEO are two important types of solid catalyst, each catalysing a broad but distinct range of chemical reactions[10–16]. Typically, $ZnCrO_x$/H-MSAPO (ref. [17]), Zn-ZrO_2/H-ZSM-5 (ref. [18]), In_2O_3/H-ZSM-5 (ref. [19]) and Cr_2O_3/H-ZSM-5 (ref. [20]) tandem catalysts were developed for direct conversion of syngas (a mixture of CO and H_2) or CO_2 into high value-added products without separating or purifying the intermediates.

An MO–ZEO composite catalyst is typically made by physically mixing the as-prepared MO nanoparticles with the ZEO component[17–20] or by an impregnation method[21,22], leading to an architecture of MO nanoparticles residing mostly randomly on the ZEO component. The consequence is, since the different active sites residing on the non-uniformly distributed MO and ZEO components are exposed to the reactants from the beginning of the reaction, that the MO- and ZEO-catalysed conversions may occur in parallel rather than in a preferred order. Moreover, given that the MO and ZEO components often catalyse the first- and second-step reactions, respectively, in the tandem catalysis for syngas and CO_2 conversion[17–20], the first-stage products formed on the MO site may easily diffuse out without further reaction on the ZEO phase. Thus, a random architecture is not beneficial to make the tandem reaction occur with the highest efficiency and desired sequence.

In this Article, we report on a generally applicable and simple synthesis method for MO@ZEO double-shelled hollow spheres (DSHSs) with predetermined metal–zeolite spatial organization and short diffusion length. The developed preparation method allows control over different structural parameters and chemical compositions. The step-by-step conversion from the precursor material to the final solid catalyst is monitored and the essential mechanisms for the involved self-assembly and hollowing behaviours are revealed. A showcase Fe_2O_3@H-ZSM-5 DSHSs material notably outperforms the conventionally synthesized and structured Fe_2O_3-H-ZSM-5 composites in gasoline production by the Fischer–Tropsch synthesis (FTS). We demonstrate that each structural engineering element in Fe_2O_3@H-ZSM-5 DSHSs, including the hollow-sphere design, Fe_2O_3@H-ZSM-5 core–shell spatial organization and "cage" effect of the H-ZSM-5 shell, contributes to the improvement of catalytic performance.

[1]Inorganic Chemistry and Catalysis, Debye Institute for Nanomaterials Science, Utrecht University, Utrecht, the Netherlands. [2]State Key Laboratory of Physical Chemistry of Solid Surfaces, College of Chemistry and Chemical Engineering, Xiamen University, Xiamen, China. [3]Soft Condensed Matter, Debye Institute for Nanomaterials Science, Utrecht University, Utrecht, the Netherlands. [4]Present address: Research Initiative for Supra-Materials, Interdisciplinary Cluster for Cutting Edge Research, Shinshu University, Nagano-shi, Japan. [5]Present address: Electron Microscopy for Materials Science (EMAT), University of Antwerp, Antwerp, Belgium. [6]Present address: Qingdao Institute of Bioenergy and Bioprocess Technology, Chinese Academy of Sciences, Qingdao, China. [7]Present address: Chemistry and Chemical Engineering, California Institute of Technology, Pasadena, CA, USA. [8]These authors contributed equally: Jiadong Xiao, Kang Cheng. ✉e-mail: wangye@xmu.edu.cn; B.M.Weckhuysen@uu.nl

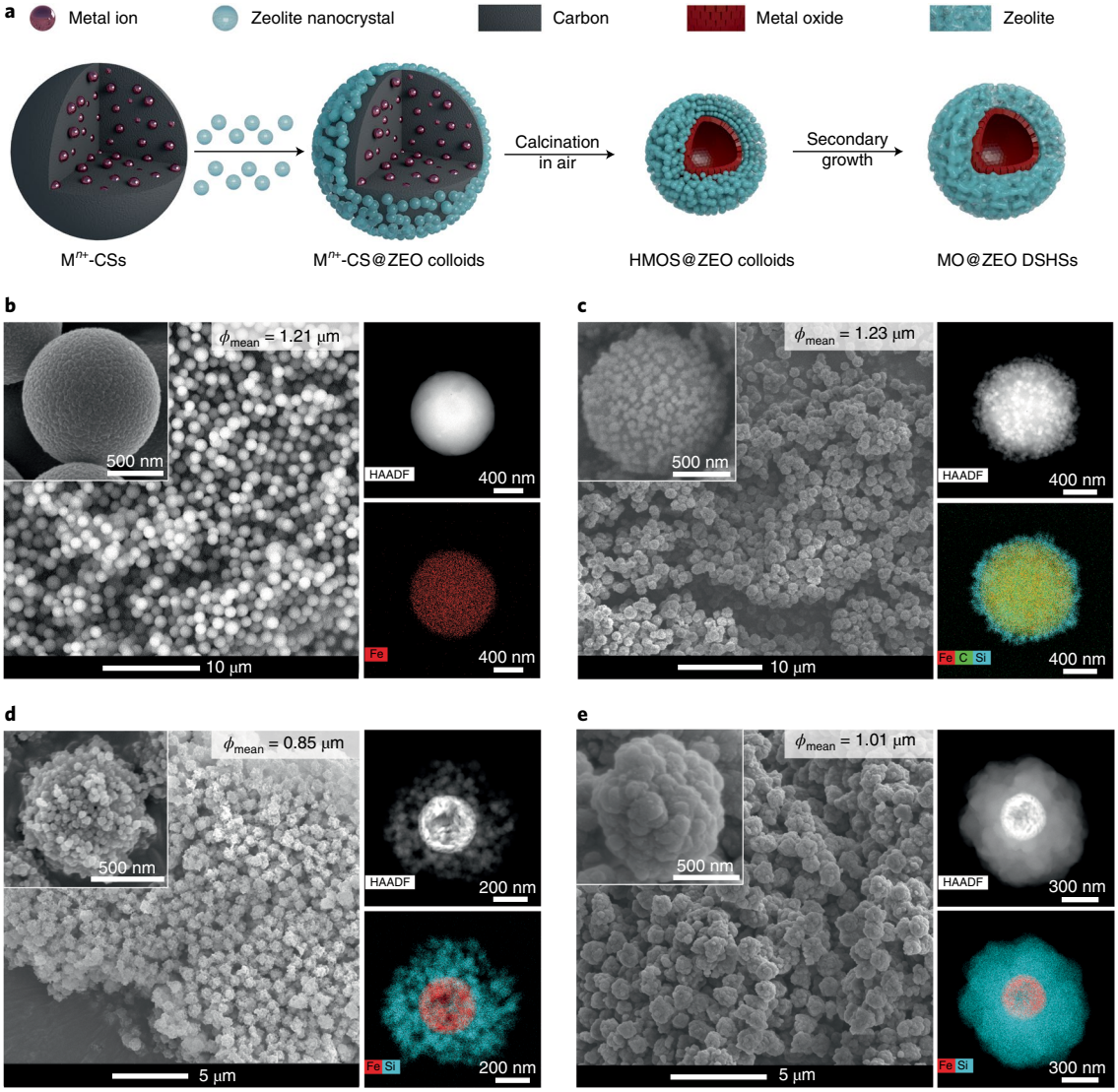

Fig. 1 | Synthesis of MO@ZEO DSHSs. a, Schematic illustration of the steps for the preparation of the MO@ZEO DSHSs material. **b**–**e**, Electron microscopy images of the intermediate/final materials during the synthesis of Fe_2O_3@S-1 DSHSs: Fe^{3+}-CSs (**b**), Fe^{3+}-CS@S-1 colloids (**c**), hollow Fe_2O_3 sphere@S-1 colloids (**d**) and Fe_2O_3@S-1 DSHSs (**e**). Each panel consists of a scanning electron microscopy (SEM) image of multiple particles (left) and a single particle (inset), a high-angle annular dark-field scanning transmission electron microscopy (STEM-HAADF) image (upper right) and an STEM image coupled with an energy-dispersive X-ray spectroscopy (STEM–EDS) elemental map (lower right) of a single particle. Φ_{mean} denotes the average external diameter of the spherical particle.

Synthesis of MO@ZEO DSHSs

The whole synthesis process (Fig. 1a, see details in Methods) involves three main steps: self-assembly attachment of zeolite nanocrystals onto the surface of metal-ion-adsorbed carbonaceous spheres (M^{n+}-CSs); calcination of M^{n+}-CS@ZEO colloids in air to form hollow MO sphere (HMOS)@ZEO colloids; and seeded growth of the zeolite nanocrystal stacked shell into a complete, fully covering shell, followed by calcination to remove the organic template in the zeolite material. M^{n+}-CSs were readily obtained by metal-cation doping of monodispersed CSs with negatively charged surfaces (ζ-potential = −18.9 mV, Supplementary Table 1) and nanopores[23], while zeolite nanocrystals with various topologies and Si/Al ratios can be synthesized by a hydrothermal method[24].

Taking the synthesis of Fe_2O_3@silicalite-1 (S-1) DSHSs as an example, simple mixing of Fe^{3+}-CSs (Fig. 1b and Supplementary Fig. 1) and S-1 nanocrystals (Φ_{mean} = 58 nm, Supplementary Fig. 2) in water with stirring led to the formation of Fe^{3+}-CS@S-1 core–shell colloidal particles, in which S-1 nanocrystals evenly attach onto the surface of the Fe^{3+}-CSs (Fig. 1c). Accordingly, very weak X-ray diffraction (XRD) peaks, assigned to S-1, were detected for this material (Fig. 2a). Further calcination of the Fe^{3+}-CS@S-1 colloidal particles in air eliminated carbon species (Fig. 2b) and formed a much smaller hollow α-Fe_2O_3 sphere (~350 nm) in place of the original solid Fe^{3+}-CS (~1,200 nm) supporting the densely stacked S-1 nanocrystals as the outer shell (Fig. 1d and Fig. 2a). This is simply due to the transformation from Fe^{3+}-CSs into hollow Fe_2O_3 spheres on calcination in air (Supplementary Fig. 3). The intensities of the XRD diffraction peaks of S-1 increased notably after this thermal treatment (Fig. 2a), due to the decomposition of CSs and the organic template in S-1.

Following a seed-assisted zeolitic growth, the zeolite nanocrystal grew up and the voids were filled such that the zeolitic shell, composed of densely stacked nanocrystals (Fig. 1d), transformed into a complete, fully covering zeolite membrane (Fig. 1e) with a

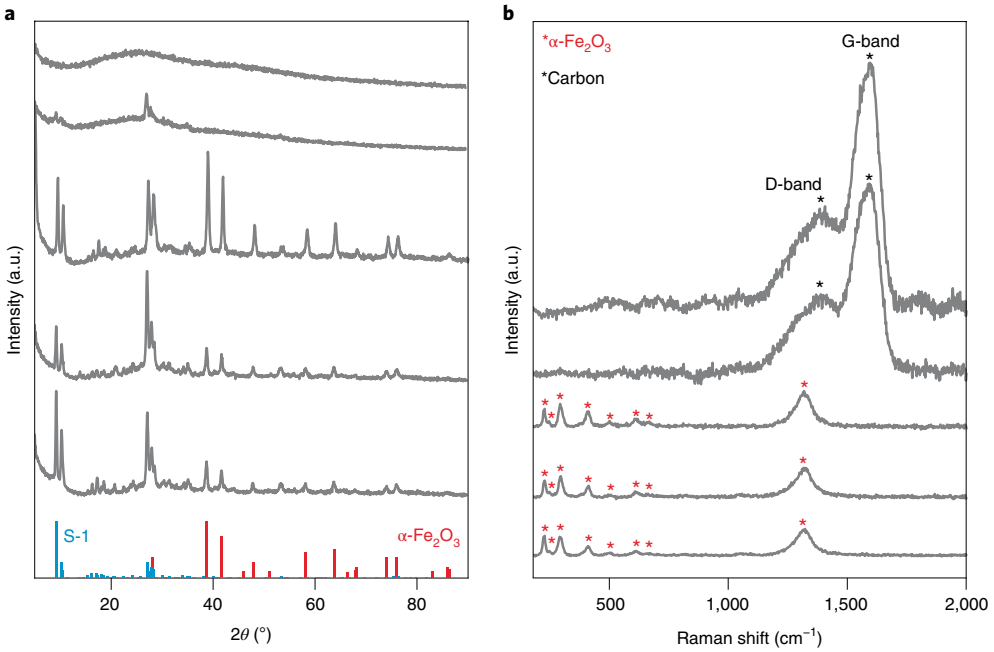

Fig. 2 | Phase variation during synthesis of Fe_2O_3@S-1 DSHSs. a,**b**, Ex situ XRD patterns (**a**) and Raman spectra (**b**) of the intermediate/final materials during the synthesis of Fe_2O_3@S-1 DSHSs. The lines from top to bottom in **a** and **b** are for Fe^{3+}-CSs, Fe^{3+}-CS@S-1 colloids, hollow Fe_2O_3 sphere@S-1 colloids and Fe_2O_3@S-1 DSHSs before and after calcination in air, respectively. The XRD standards for α-Fe_2O_3 and S-1 in **a** correspond to JCPDS numbers 33-0664 (red) and 48-0136 (cyan), respectively.

slightly increased thickness (Supplementary Fig. 4). This corroborates the increase in the XRD peak intensity ratio of S-1 to α-Fe_2O_3 (Fig. 2a). Annealing in air was finally required to oxidatively decompose the organic template in the S-1 shell. This step had, fortunately, no impact on the overall material architecture, but led to some variations of the XRD peak intensities for S-1 (Fig. 2a). The resulting Fe_2O_3@S-1 DSHSs are spherical particles with diameters of ~1 μm (Supplementary Fig. 4d) and every particle comprises a hollow Fe_2O_3 sphere as the core and a hollow S-1 sphere as the shell (Fig. 1e and Supplementary Figs. 5 and 6). Accordingly, this material has a Brunauer–Emmett–Teller specific surface area (S_{BET}) of 343 m^2 g^{-1} and micro-pores of 198 m^2 g^{-1} arising from the S-1 shell (Supplementary Fig. 7). The Fe_2O_3@S-1 DSHSs exhibited an excellent structural stability under ultrasonic or steaming treatment (Supplementary Fig. 8). Note that solid sphere-like zeolite particles primarily formed following the same procedures while using CSs as the template (Supplementary Fig. 9).

Growth mechanism for MO@ZEO DSHSs

Throughout the synthesis, doping CSs with the metal cation solution for producing M^{n+}-CSs and seeded growth of the zeolite shell are readily comprehensible, but the self-assembly behaviour between zeolite nanocrystals and M^{n+}-CSs as well as the hollowing mechanism of MO remain ambiguous. Electrostatic attraction between oppositely charged species can be excluded because both the Fe^{3+}-CSs (ζ-potential = −13.5 mV) and S-1 nanocrystals (ζ-potential = −14.4 mV) exhibited slightly negatively charged surfaces (Supplementary Table 1). It is known that the Hamaker constants that describe the van der Waals attractions[25] are roughly an order of magnitude larger for the Fe^{3+}-CSs. Thus, at the relatively high ion strength present in the solution, the double-layer repulsion is reduced and aggregation induced by the van der Waals attractions between the nanocrystals and Fe^{3+}-CSs was found to occur. Once collisions occurred between the S-1 nanocrystals and particles of Fe^{3+}-CSs, hydrogen bonding (Supplementary Fig. 10) also contributed to their aggregation[26]. Once the Fe^{3+}-CSs were coated by a thick layer of zeolite nanocrystals, colloidal stability was restored and the aggregation was terminated.

To understand the transformation from Fe^{3+}-CSs@S-1 colloids (Fig. 1c) into hollow α-Fe_2O_3 sphere@S-1 particles (Fig. 1d), in situ Raman spectroscopy (Fig. 3a) and XRD diffraction (Fig. 3b,c and Supplementary Fig. 11) were used to monitor the decomposition of the carbonaceous species and the crystalline phase transitions of the iron and zeolitic components, respectively. The Raman signals of the G- and D-bands weakened with increasing temperature and disappeared at around 260 °C (Fig. 3a), indicating the gradual decomposition of CSs (ref. [27]). Accordingly, we observed a shrinkage of the cores from initially 1,222 nm (Fig. 3d) to 767 nm (Fig. 3e) at 210 °C and the formation of a solid, amorphous FeO_x core ($\Phi \approx 350$ nm) at 270 °C (Fig. 3b,f). With increasing temperature from 270 to 400 °C, we observed the gradual morphological variation of the FeO_x core from a solid sphere at 270 °C (Fig. 3f) to a hollow sphere with a shell thickness of ~120 nm at 350 °C (Fig. 3g) and further into a denser and hollower sphere with an ~70 nm shell thickness at 400 °C (Fig. 3h). The dense, hollow sphere at 400 °C was almost identical to the final shape observed at 500 °C (Fig. 3i). Meanwhile, a slow increase in the XRD peak area at $2\theta = 38.7°$ was found from 270 to 400 °C, indicating that a handful of polycrystalline α-Fe_2O_3 nanocrystals had already formed at this heating stage.

In the cross-sectional specimen of the sample at the heating point of 400 °C (Fig. 3j and Fig. 3k), the three sites selected in a nearly radial direction were notably different in their crystalline states. Site l (Fig. 3l), which is close to the surface, was highly crystalline, but the interior of the shell imaged at site n (Fig. 3n) was almost amorphous. The intermediate site m (Fig. 3m) was a transition zone, showing a discernible borderline (illustrated by a white dashed line) between crystalline and amorphous regions. This border was expected to move further inside with increasing temperature from 400 to 476 °C, leading to an expansion of the crystalline area to the whole particle (Fig. 3c). A crystal phase usually has a notably higher

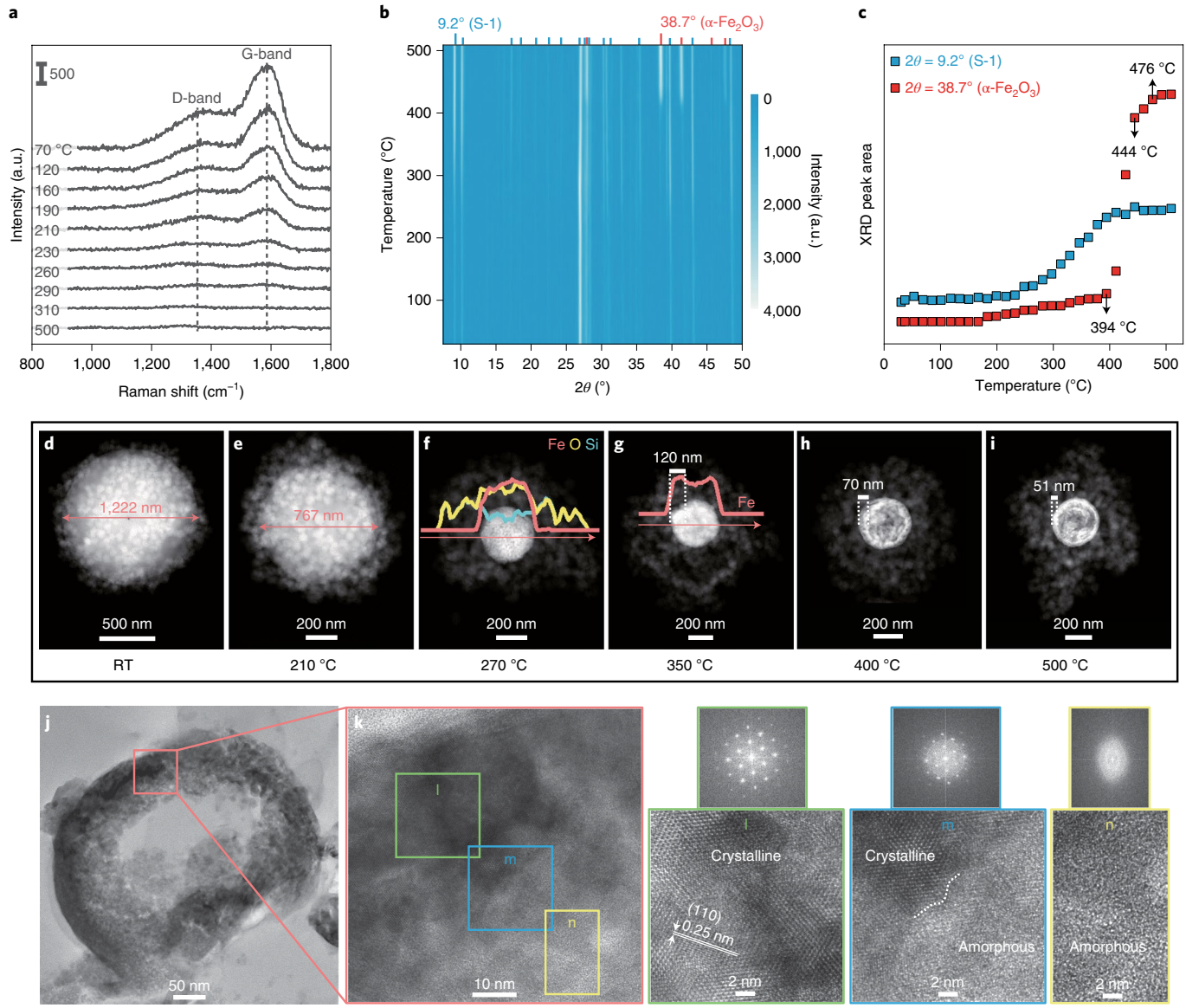

Fig. 3 | Monitoring of the transformation from an Fe^{3+}-CS@S-1 colloid to a hollow Fe_2O_3 sphere@S-1 colloid during calcination in air. a,**b**, In situ Raman spectra (**a**) and 2D contour plot showing the in situ XRD intensities as functions of 2θ and the temperature (**b**) during calcining of Fe^{3+}-CS@S-1 colloids under static air or in the O_2/Ar (1/4, v/v) gas flow. **c**, Changes of the XRD peak areas at 2θ of 9.2° and 38.7° as a function of the temperature during the in situ XRD measurement. **d**–**i**, Ex situ STEM-HAADF images (with or without EDS line-scan spectra) of Fe^{3+}-CS@S-1 colloids (**d**) and of the resulting material on calcining Fe^{3+}-CS@S-1 colloids in air up to 210 °C (**e**), 270 °C (**f**), 350 °C (**g**), 400 °C (**h**) and 500 °C (**i**) with a rate of 1 °C min^{-1}. Once the target temperature was reached, the sample was immediately taken out for rapid cooling and analysis. RT, room temperature. **j**,**k**, Bright-field transmission electron microscopy (TEM) (**j**) and high-resolution TEM (HRTEM) images (**k**) of a cross-sectional sample of the material in **h**. **l**–**n** Enlarged HRTEM images (bottom) and the corresponding Fourier transform patterns (top) of the selected areas in **k**.

density compared to its amorphous counterpart[28], so it is plausible that two trends, namely inward crystallization and outward contraction, occurred almost simultaneously, resulting in gradual hollowing from the centre and diffusion of the crystalline region inward. This is reminiscent of the Kirkendall effect[29,30], in which different inter-diffusion rates of two different materials/phases lead to both boundary motion and vacancy enrichment. The transformation of a kinetically unstable amorphous phase into the more stable crystalline phase here involved the dissolution and recrystallization of an unstable phase, showing also some characteristics of Ostwald ripening growth[30,31]. Therefore, the hollowing process may involve both Kirkendall and Ostwald ripening mechanisms.

Structure and composition of MO@ZEO DSHSs

The thickness of the S-1 shell could be tuned from 139 to 283 and further to 400 nm, on adding 2.5, 15 and 25 ml 1 wt% S-1 nanocrystal suspension for each gram of Fe^{3+}-CSs (Fig. 4a–d and Supplementary Fig. 12). In comparison, the extension of the secondary growth time caused only slight thickening of the zeolite shell (Supplementary Fig. 13). The thickness of the hollow MO sphere increased with the concentration of the metal precursor doping solution (Fig. 4e–h and Supplementary Fig. 14). Note that concentrating the $Fe(NO_3)_3$ doping solution from 1.5 to 2.5 M did not increase the Fe_2O_3 shell thickness further, but created a double-shelled Fe_2O_3 hollow sphere architecture for the majority of the particles obtained (Fig. 4g and

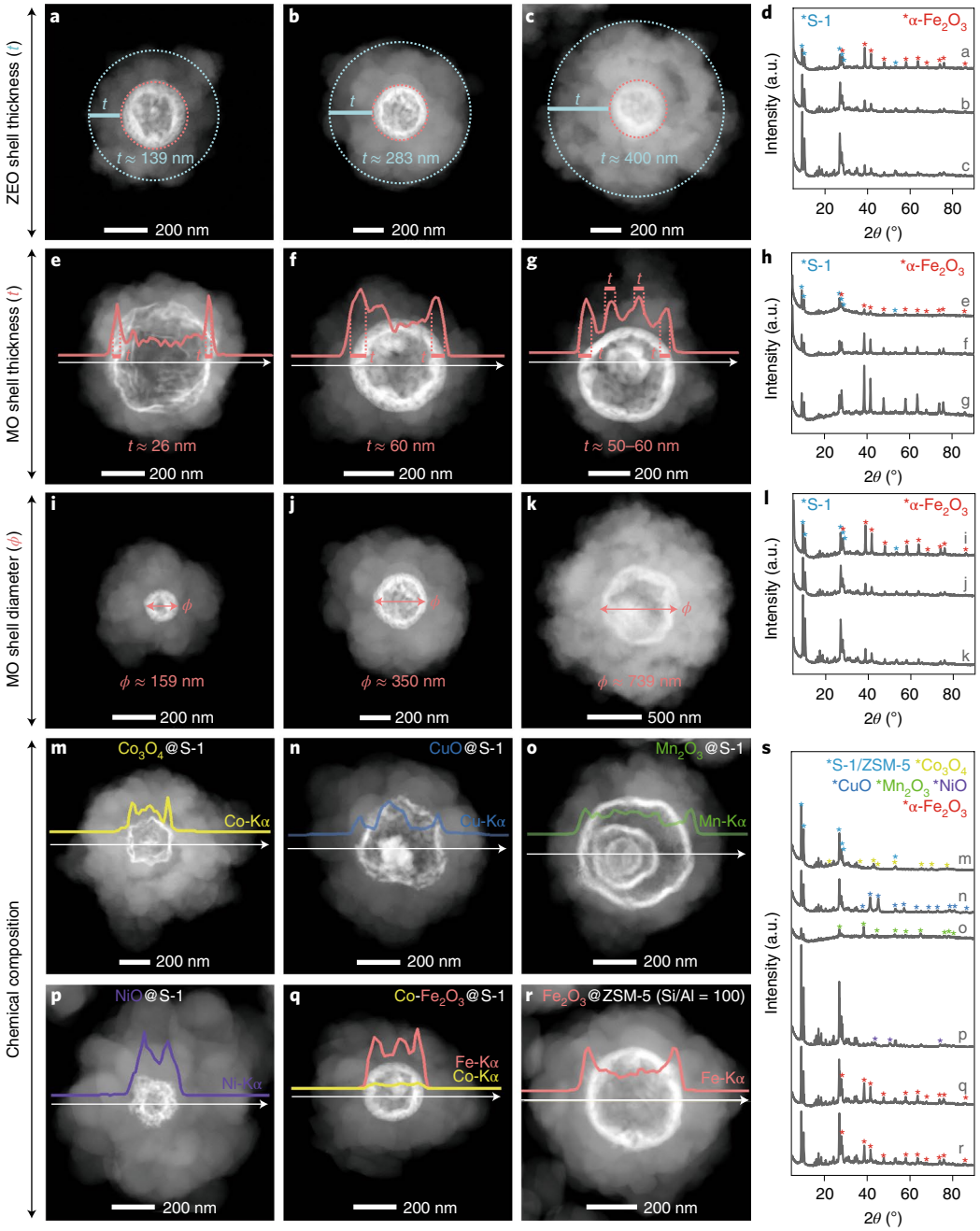

Fig. 4 | Manipulation of structural parameters and chemical compositions in MO@ZEO DSHSs. a–c, STEM-HAADF images of a single Fe_2O_3@S-1 DSHS particle with a S-1 shell thickness (t) of around 139 nm (**a**), 283 nm (**b**) and 400 nm (**c**). **d**, XRD patterns of the materials in **a**–**c**. **e**–**g**, STEM-HAADF images of a single Fe_2O_3@S-1 DSHS particle with an Fe_2O_3 shell thickness of around 26 nm (**e**), 60 nm (**f**) and with double Fe_2O_3 shells (**g**). **h**, XRD patterns of the materials in **e**–**g**. **i**–**k**, STEM-HAADF images of a single Fe_2O_3@S-1 DSHS particle with an external Fe_2O_3 shell diameter of around 159 nm (**i**), 350 nm (**j**) and 739 nm (**k**). Note that **b** and **j** show the same particle, and this material is also imaged in Fig. 1e. **l**, XRD patterns of the materials in **i**–**k**. **m**–**r**, STEM-HAADF images of a single Co_3O_4@S-1 DSHS (**m**), CuO@S-1 DSHS (**n**), Mn_2O_3@S-1 multi-shelled hollow sphere (MSHS) (**o**), NiO@S-1 DSHS (**p**), Co-Fe_2O_3@S-1 DSHS (**q**) and Fe_2O_3@ZSM-5 (Si/Al = 100) DSHS (**r**) particle. **s**, XRD patterns of the materials in **m**–**r**.

Supplementary Fig. 14c). This is because the outer parts of the Fe species are sufficient to form the first outer Fe_2O_3 shell and the different rates of MO formation and disintegration of CSs cause the spatial separation between the newly formed MO shell and shrinking M^{n+}-CSs that further forms the inner Fe_2O_3 shell[32,33]. The utilization of 0.4, 1.2 and 2.4 μm CSs generates Fe_2O_3@S-1 DSHSs with diameters of the Fe_2O_3 shell at approximately 160, 350 and 740 nm, respectively (Fig. 4i–l and Supplementary Fig. 15), indicating that the hollow MO sphere diameter was governed by the size of CSs (Supplementary Fig. 16). Thus, the whole particle size could be controlled by manipulating the diameter of the MO shell and the thickness of the ZEO shell.

The chemical composition of the MO shell was governed by the metal precursor in the doping solution (Fig. 4m–s). Co_3O_4 (Fig. 4m and Supplementary Fig. 17), CuO (Fig. 4n and Supplementary Fig. 18), Mn_2O_3 (Fig. 4o and Supplementary Fig. 19), NiO (Fig. 4p and Supplementary Fig. 20), Co-doped Fe_2O_3 (Fig. 4q and Supplementary Fig. 21) and $NiCo_2O_4$ (Supplementary Fig. 22) hollow spheres were

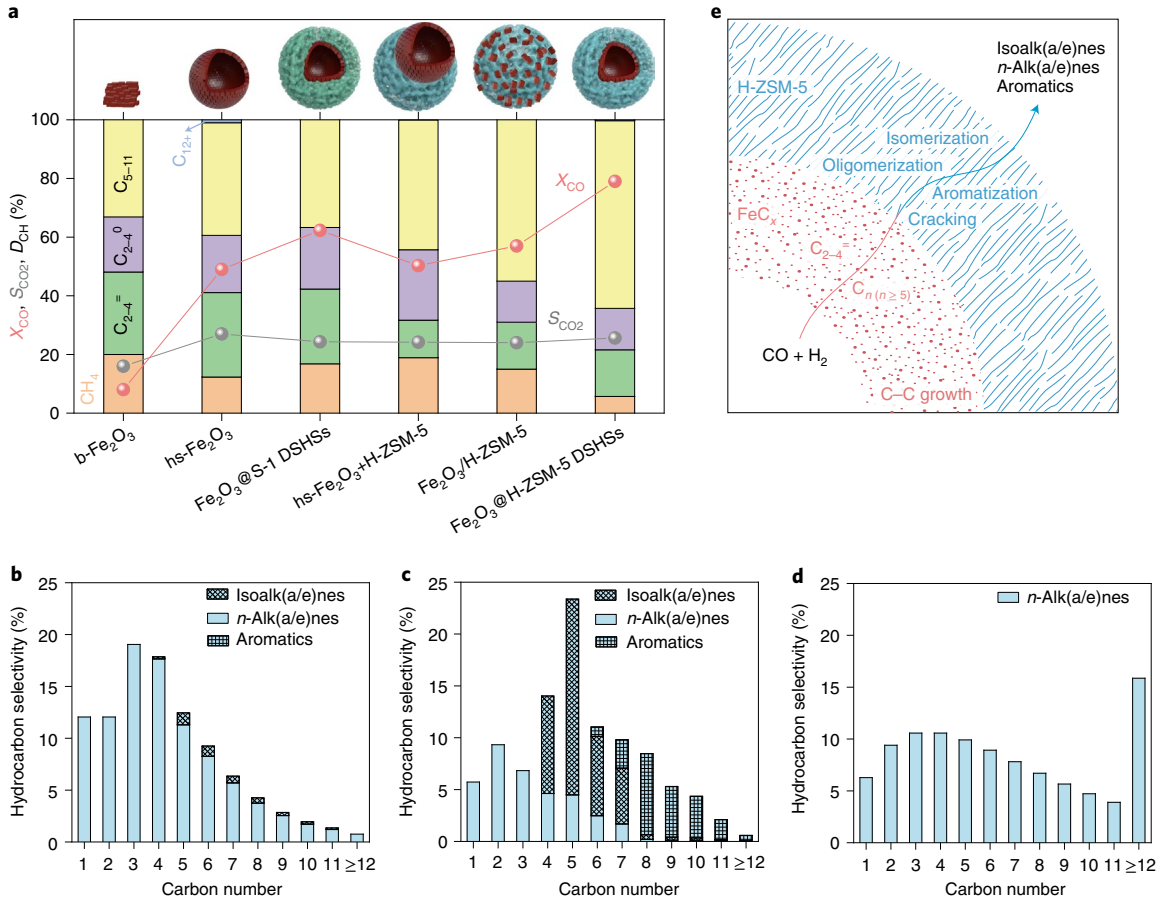

Fig. 5 | Catalytic performances of different catalyst materials in syngas conversion. a, CO conversion (X_{co}), CO_2 selectivity (S_{CO2}) and distribution of hydrocarbon products (D_{CH}) in syngas conversion catalysed by b-Fe_2O_3, hs-Fe_2O_3, Fe_2O_3@S-1 DSHSs, hs-Fe_2O_3+H-ZSM-5, Fe_2O_3/H-ZSM-5 and Fe_2O_3@H-ZSM-5 DSHSs. The top images show the structural model of each catalyst. **b**,**c**, Detailed hydrocarbon distributions in syngas conversion over hs-Fe_2O_3 (**b**) and Fe_2O_3@H-ZSM-5 DSHSs (**c**). **d**, Theoretical ASF distribution with an alpha value of 0.75. **e**, Schematic illustration of the C_5–C_{11} hydrocarbon formation pathway on Fe_2O_3@H-ZSM-5 DSHSs. Reaction conditions: W_{cat} = 0.03 (for catalysts without acid sites) or 0.3 g (for bifunctional catalysts), H_2/CO = 2/1, F_{syngas} = 30 ml min^{-1}, T = 300 °C, P = 3 MPa, time on stream = 15 h. The catalyst was reduced by H_2 at 400 °C for 2 h before the atmosphere was switched to the reaction feed gas. Detailed catalytic performance data are shown in Supplementary Table 2.

formed inside the S-1 shell, on doping CSs with the specific precursor solution. The Si/Al ratio and topology of the ZEO shell can be tuned by using well-matched ZEO nanocrystals[24] and performing the secondary zeolitic growth in a proper manner. Fe_2O_3@ZSM-5 DSHSs with Si/Al ratios of ~100 (Fig. 4r and Supplementary Fig. 23) were synthesized using ZSM-5 nanocrystals (Supplementary Fig. 24) with a Si/Al ratio of 100. Note that the lowest Si/Al ratio attainable in Fe_2O_3@ZSM-5 DSHSs was 50 (Supplementary Fig. 25). The attainability of CuO@Si-Beta zeolite DSHSs (Supplementary Fig. 26) indicates that the fabrication of MO@ZEO DSHSs with other zeolitic topologies (for example, FAU, LTA, SOD and MOR (ref. [24])) is feasible.

Tandem catalysis with MO@ZEO DSHSs

Taking FTS as the model tandem reaction, the performances of bulk Fe_2O_3 (b-Fe_2O_3, Supplementary Fig. 27), hollow-sphere Fe_2O_3 (hs-Fe_2O_3, Supplementary Fig. 3), Fe_2O_3@S-1 DSHSs (Fig. 1e and Supplementary Fig. 5), hs-Fe_2O_3+H-ZSM-5 (prepared by physical mixing of hs-Fe_2O_3 and H-ZSM-5), Fe_2O_3/H-ZSM-5 (prepared by an impregnation method, Supplementary Fig. 28) and Fe_2O_3@H-ZSM-5 DSHSs (Fig. 4r and Supplementary Fig. 23) were evaluated under industrially relevant conditions (Fig. 5 and Supplementary Table 2). As shown in Fig. 5a, b-Fe_2O_3, hs-Fe_2O_3 and Fe_2O_3@S-1 DSHSs exhibited very similar product distribution and a limited selectivity for C_5–C_{11} hydrocarbons (33–38%), while the CO conversion efficiencies varied widely. The dispersion of iron species reflected by S_{BET} (Supplementary Table 3) was higher in hs-Fe_2O_3 (61.2 m^2 g^{-1}) than in b-Fe_2O_3 (18.1 m^2 g^{-1}). Consequently, hs-Fe_2O_3 (X_{co} = 49.0%) caused far more efficient conversion of CO than b-Fe_2O_3 (X_{co} = 8.0%). The CO conversion ratio was further improved from 49.0 to 62.3% when encapsulating hs-Fe_2O_3 with a S-1 layer. This is likely to be due to the enrichment of reagents by the hollow S-1 sphere.

Combining H-ZSM-5 with Fe_2O_3 to form a tandem catalyst effectively improved the selectivity for C_5–C_{11} hydrocarbons (Fig. 5 and Supplementary Table 2). By physically mixing hs-Fe_2O_3 with H-ZSM-5 (Supplementary Fig. 9), the C_5–C_{11} hydrocarbon selectivity was improved from 38.4% for hs-Fe_2O_3 to 44.2% for hs-Fe_2O_3+H-ZSM-5. Fe_2O_3/H-ZSM-5 exhibited higher CO conversion (57.0%) and C_5–C_{11} hydrocarbon selectivity (55.0%) compared with hs-Fe_2O_3+H-ZSM-5, while the most active was the Fe_2O_3@H-ZSM-5 DSHSs catalyst, exhibiting a CO conversion level and C_5–C_{11} hydrocarbon selectivity of 79.0 and 64%, respectively. As experimentally indicated by the decrease in the $C_{2-4}^{=}$ (C_2–C_4 olefins) selectivity from 28.8% for hs-Fe_2O_3 to 15.9% for Fe_2O_3@H-ZSM-5 DSHSs (Fig. 5a) and by the increase in the fractions of isohydrocarbons and aromatics within the

C_5–C_{11} products (Fig. 5b,c), the improvement over the bifunctional catalyst mainly results from the oligomerization of linear alkenes catalysed by the acidic zeolite component followed by isomerization, aromatization and cracking (Fig. 5e)[34,35]. The obtained C_5–C_{11} hydrocarbon selectivity and composition of Fe_2O_3@H-ZSM-5 DSHSs (Fig. 5c) was notably beyond the upper limit of the Anderson–Schulz–Flory (ASF) theory (Fig. 5d). Note that these differently structured bifunctional catalysts have an almost identical S_{BET} (Supplementary Table 3), acidic property (Supplementary Figs. 29 and 30) and Fe_2O_3/H-ZSM-5 mass ratio (~1:9), and that the latter property was optimized for Fe_2O_3@H-ZSM-5 DSHSs (Supplementary Table 4 and Supplementary Figs. 31 and 32). Although the C_5–C_{11} selectivity (64.0%) of Fe_2O_3@H-ZSM-5 DSHSs is slightly lower than that of the best-in-class Fe_3O_4@MnO_2+Hol-H-ZSM-5 catalyst[34,36], the composition of the produced C_5–C_{11} liquid hydrocarbons is much closer to the required standard of practical gasoline (see detailed explanation below Supplementary Table 5).

The content of formed iron carbides (FeC_x) in the catalysts used for 45 h on stream followed the order hs-Fe_2O_3+H-ZSM-5 > Fe_2O_3@H-ZSM-5 DSHSs > Fe_2O_3/H-ZSM-5 (Supplementary Fig. 33 and Supplementary Table 6), in line with the reducibility of Fe_2O_3 in these materials (Supplementary Fig. 34). This order is the consequence of the degree of iron dispersion and the spatial/chemical interaction between iron species and H-ZSM-5 (see detailed explanation below Supplementary Table 6). It was not unexpected that Fe_2O_3/H-ZSM-5, having fewer FeC_x, performed worse than Fe_2O_3@H-ZSM-5 DSHSs. Although the FeC_x content was the highest in hs-Fe_2O_3+H-ZSM-5, the FTS performance was inferior to that of Fe_2O_3@H-ZSM-5 DHSHs and Fe_2O_3/H-ZSM-5 (Fig. 5a). It is most likely to be as a result of the excess separation of the metal and acid sites that the formation of C_2–C_4 alkanes from hydrogen transfer or cracking became favourable and restricted the formation of C_5–C_{11} hydrocarbons. In addition to forming a moderate amount of FeC_x, the core–shell hollow-sphere design of Fe_2O_3@H-ZSM-5 DSHSs led to an appropriate contact between highly dispersed metal and acid sites and assured a whole journey of a tandem reaction. Moreover, the hollow H-ZSM-5 sphere in Fe_2O_3@H-ZSM-5 DSHSs could enrich the reactants (Supplementary Fig. 35) and reaction intermediates (Supplementary Fig. 36) around the active sites. All these properties arising from the architecture made Fe_2O_3@H-ZSM-5 DSHSs stand out in gasoline production by FTS.

Fe_2O_3@H-ZSM-5 DSHSs worked stably after a short induction time of 10 h and no catalyst deactivation was observed during 45 h on stream (Supplementary Fig. 37 and Supplementary Table 7). The catalyst particles maintained their physical integrities after FTS for 45 h and the hollow ferruginous spheres remained intact. This is likely due to the confinement/protection of the zeolite shell, although the ferruginous sphere turned out to be more porous than fresh catalyst (Supplementary Fig. 38a,b). Following a regeneration process (annealing at 500 °C in air for 2 h), the catalyst particles almost restored their initial structure (Supplementary Fig. 38c).

This work provides a new configuration of metal– or metal oxide–zeolite bifunctional catalysts compared with the existing ones in bifunctional systems (Supplementary Fig. 39) and demonstrates the importance of structural engineering at different length scales to the performance of solid catalysts. The universal synthesis method and the material growth mechanism revealed here would advance the research of hierarchically hollow, core–shell materials and the understanding of self-assembly and hollowing processes. The diverse MO@ZEO DSHSs produced are expected to be useful for a variety of catalytic reactions beyond FTS.

Online content

Any methods, additional references, Nature Research reporting summaries, source data, extended data, supplementary information, acknowledgements, peer review information; details of author contributions and competing interests; and statements of data and code availability are available at https://doi.org/10.1038/s41563-021-01183-0.

Received: 13 December 2020; Accepted: 2 December 2021;
Published online: 27 January 2022

References

1. Yang, P. & Tarascon, J.-M. Towards systems materials engineering. *Nat. Mater.* **11**, 560–563 (2012).
2. Zhu, Y. et al. Structural engineering of 2D nanomaterials for energy storage and catalysis. *Adv. Mater.* **30**, 1706347 (2018).
3. Parlett, C. M. A. et al. Spatially orthogonal chemical functionalization of a hierarchical pore network for catalytic cascade reactions. *Nat. Mater.* **15**, 178–182 (2016).
4. Isaacs, M. A. et al. A spatially orthogonal hierarchically porous acid-base catalyst for cascade and antagonistic reactions. *Nat. Catal.* **3**, 921–931 (2020).
5. Cho, H. J., Kim, D., Li, J., Su, D. & Xu, B. Zeolite-encapsulated Pt nanoparticles for tandem catalysis. *J. Am. Chem. Soc.* **140**, 13514–13520 (2018).
6. Cheng, K. et al. Impact of the spatial organization of bifunctional metal-zeolite catalysts for hydroisomerization of light alkanes. *Angew. Chem. Int. Ed.* **59**, 3592–3600 (2020).
7. Climent, M. J., Corma, A., Iborra, S. & Sabater, M. J. Heterogeneous catalysis for tandem reactions. *ACS Catal.* **4**, 870–891 (2014).
8. Behr, A., Vorholt, A. J., Ostrowski, K. A. & Seidensticker, T. Towards resource efficient chemistry: tandem reactions with renewables. *Green Chem.* **16**, 982–1006 (2014).
9. Lohr, T. L. & Marks, T. J. Orthogonal tandem catalysis. *Nat. Chem.* **7**, 477–482 (2015).
10. Védrine, J. C. Metal oxides in heterogeneous oxidation catalysis: state of the art and challenges for a more sustainable world. *ChemSusChem* **12**, 577–588 (2019).
11. De Jong, K. P. in *Synthesis of Solid Catalysts* (ed. De Jong, K. P.) 3–12 (Wiley-VCH, 2009).
12. Chen, S., Takata, T. & Domen, K. Particulate photocatalysts for overall water splitting. *Nat. Rev. Mater.* **2**, 17050 (2017).
13. Hong, W. T. et al. Toward the rational design of non-precious transition metal oxides for oxygen electrocatalysis. *Energy Environ. Sci.* **8**, 1404–1427 (2015).
14. Corma, A. From microporous to mesoporous molecular sieve materials and their use in catalysis. *Chem. Rev.* **97**, 2373–2420 (1997).
15. Vogt, E. T. C. & Weckhuysen, B. M. Fluid catalytic cracking: recent developments on the grand old lady of zeolite catalysis. *Chem. Soc. Rev.* **44**, 7342–7370 (2015).
16. Li, Y., Li, L. & Yu, J. Applications of zeolites in sustainable chemistry. *Chem* **3**, 928–949 (2017).
17. Jiao, F. et al. Selective conversion of syngas to light olefins. *Science* **351**, 1065–1068 (2016).
18. Cheng, K. et al. Bifunctional catalysts for one-step conversion of syngas into aromatics with excellent selectivity and stability. *Chem* **3**, 334–347 (2017).
19. Gao, P. et al. Direct conversion of CO_2 into liquid fuels with high selectivity over a bifunctional catalyst. *Nat. Chem.* **9**, 1019–1024 (2017).
20. Wang, Y. et al. Rationally designing bifunctional catalysts as an efficient strategy to boost CO_2 hydrogenation producing value-added aromatics. *ACS Catal.* **9**, 895–901 (2019).
21. Takeuchi, M., Kimura, T., Hidaka, M., Rakhmawaty, D. & Anpo, M. Photocatalytic oxidation of acetaldehyde with oxygen on TiO_2/ZSM-5 photocatalysts: effect of hydrophobicity of zeolites. *J. Catal.* **246**, 235–240 (2007).
22. Huang, H. et al. Catalytic oxidation of benzene over Mn modified TiO_2/ZSM-5 under vacuum UV irradiation. *Appl. Catal. B* **203**, 870–878 (2017).
23. Wang, Q., Li, H., Chen, L. & Huang, X. Monodispersed hard carbon spherules with uniform nanopores. *Carbon* **39**, 2211–2214 (2001).
24. Tosheva, L. & Valtchev, V. P. Nanozeolites: synthesis, crystallization mechanism, and applications. *Chem. Mater.* **17**, 2494–2513 (2005).
25. Israelachvili, J. N. in *Intermolecular and Surface Forces* 3rd edn (ed. Israelachvili, J. N.) 253–340 (Academic Press, 2011).
26. Lee, J. S., Kim, J. H., Lee, Y. J., Jeong, N. C. & Yoon, K. B. Manual assembly of microcrystal monolayers on substrates. *Angew. Chem. Int. Ed.* **46**, 3087–3090 (2007).
27. Kudin, K. N. et al. Raman spectra of graphite oxide and functionalized graphene sheets. *Nano Lett.* **8**, 36–41 (2008).
28. Li, Y., Guo, Q., Kalb, J. & Thompson, C. Matching glass-forming ability with the density of the amorphous phase. *Science* **322**, 1816–1819 (2008).
29. Yin, Y. et al. Formation of hollow nanocrystals through the nanoscale Kirkendall effect. *Science* **304**, 711–714 (2004).

30. Yang, L.-P. et al. General synthetic strategy for hollow hybrid microspheres through a progressive inward crystallization process. *J. Am. Chem. Soc.* **138**, 5916–5922 (2016).
31. Cao, L., Chen, D. & Caruso, R. A. Surface-metastable phase-initiated seeding and ostwald ripening: a facile fluorine-free process towards spherical fluffy core/shell, yolk/shell, and hollow anatase nanostructures. *Angew. Chem. Int. Ed.* **52**, 10986–10991 (2013).
32. Lai, X. et al. General synthesis and gas-sensing properties of multiple-shell metal oxide hollow microspheres. *Angew. Chem. Int. Ed.* **50**, 2738–2741 (2011).
33. Wang, J. Y., Wan, J. W. & Wang, D. Hollow multishelled structures for promising applications: understanding the structure–performance correlation. *Acc. Chem. Res.* **52**, 2169–2178 (2019).
34. Xu, Y. et al. Selective conversion of syngas to aromatics over Fe_3O_4@MnO_2 and hollow HZSM-5 bifunctional catalysts. *ACS Catal.* **9**, 5147–5156 (2019).
35. Zhao, B. et al. Direct transformation of syngas to aromatics over Na-Zn-Fe_5C_2 and hierarchical HZSM-5 tandem catalysts. *Chem* **3**, 323–333 (2017).
36. Xu, Y., Wang, J., Ma, G., Lin, J. & Ding, M. Designing of hollow ZSM-5 with controlled mesopore sizes to boost gasoline production from syngas. *ACS Sustain. Chem. Eng.* **7**, 18125–18132 (2019).

Methods

Synthesis of CSs and M^{n+}-CSs. The CSs were synthesized by hydrothermal polymerization of sucrose, as reported elsewhere[23]. Typically, 60 ml sucrose solution (1.5 M) was hydrothermally treated at 190 °C for 110 min in a 120 ml Teflon-lined stainless steel autoclave. After washing with distilled water, ethanol and acetone, dark brown CSs were collected and dried at 100 °C for further use. Metal cation adsorbed CSs (M^{n+}-CSs) were obtained by doping CSs with an aqueous solution of the metal precursor. In a typical run for synthesizing Fe^{3+}-CSs, freshly-made CSs (0.5 g) were dispersed by ultrasonication for 15 min in 1.5 M ferric nitrate solution (distilled water/ethanol = 1:1, v/v, 20 ml). The suspension was then aged for 5 h under magnetic stirring at room temperature. Following rinsing and drying, Fe^{3+}-CSs were obtained. Other M^{n+}-CSs can be obtained by a similar procedure.

Synthesis of MFI-topology and BEA-topology zeolite nanocrystals. MFI zeolite nanocrystals with different Si/Al ratios were synthesized by a reported method with some modifications[37,38]. Typically for synthesizing nanocrystalline ZSM-5 (for example with Si/Al = 100), aluminium isopropoxide (AlP) was transferred to a polypropylene bottle containing tetrapropylammonium hydroxide (TPAOH, 1 M in H_2O). The solution was stirred at room temperature for about 30 min to get a clear solution. Tetraethoxysilane (TEOS) was added to this solution followed by distilled water. The resulting solution was stirred vigorously at room temperature for about 2 h to hydrolyse the TEOS. The molar composition of the final solution (pH ≈ 11.4) was 1 SiO_2/0.01 AIP/0.25 TPAOH/4 EtOH/20 H_2O. The clear sol was concentrated by evaporation at 80 °C under stirring in a beaker until the H_2O/SiO_2 molar ratio in the sol reached about 4.20. The concentrated sol was further hydrothermally treated at 180 °C for 90 min in a Teflon-lined stainless steel autoclave. After washing with distilled water 3 times using centrifugation at a speed of 16,369*g* (Rotina 380 R, Hettich), hydrous ZSM-5 (Si/Al = 100) nanocrystals (1 g) were finally dispersed in distilled water (99 ml) to produce an ~1 wt% aqueous suspension which could be stable for several months. Note that desiccated zeolite nanocrystals cannot be redispersed in water to form a stable suspension. Silicallite-1 (S-1, Si/Al = ∞) nanocrystals were obtained by similar procedures without adding AIP. Si-Beta zeolite (Si/Al = ∞) nanocrystals were synthesized from a clear precursor sol having the chemical composition of 1 SiO_2/0.028 NaOH/0.36 TEAOH/11.8 H_2O, as modified from Yordanov et al[39]. Fumed silica (CAB-O-SIL M5) was used as the silica source and tetraethylammonium hydroxide (TEAOH, 35 wt% in H_2O) was used as the organic structure-directing agent and template. The precursor suspension was aged at room temperature for 3 days prior to further hydrothermal treatment in a Teflon-lined stainless steel autoclave at 100 °C for 3 days. After washing with distilled water 3 times using centrifugation at a speed of 16,369*g* (Rotina 380 R, Hettich), Si-Beta zeolite (Si/Al = ∞) nanocrystals were finally dispersed in distilled water to produce an ~1 wt% suspension for storage.

Synthesis of MO@ZEO DSHSs. For the typical synthesis of Fe_2O_3@S-1 DSHSs, a certain volume (for example, 0.15, 1.5 or 2.5 ml) of 1 wt% S-1 nanocrystal suspension was slowly added to an suspension of aqueous Fe^{3+}-CSs (1 mg ml^{-1}) under stirring. Following stirring for 0.5 h, the aqueous suspension was subjected to a low-speed centrifugation treatment at 541*g* (Rotina 380 R, Hettich) for 5 min, to remove the unattached S-1 nanocrystals. The material (that is, Fe^{3+}-CSs@S-1 colloidal particles) was collected and further calcined in static air at 500 °C for 1 h with a ramping rate of 1 °C min^{-1}. The resulting material (that is, hollow Fe_2O_3 sphere@S-1 colloids; 0.15 g) was further dispersed in an as-prepared sol (15 ml) having the chemical composition of 1 SiO_2/0.12 TPAOH/60 H_2O/4 EtOH (TEOS was used as the Si source), with the assistance of brief sonication. The suspension was then transferred to a tightly closed polypropylene bottle and hydrothermally treated at 95 °C for 24 h under magnetic stirring in an oil bath. After washing, drying and further calcination of the solid in static air at 550 °C for 6 h with a ramping rate of 2 °C min^{-1}, Fe_2O_3@S-1 DSHSs were finally obtained. Other MO@ZEO DSHSs were synthesized using similar procedures. For synthesizing Fe_2O_3@ZSM-5 DSHSs (Si/Al ≈ 100), ZSM-5 (Si/Al = 100) nanocrystals were used and the secondary growth sol was composed of 1 SiO_2/0.01 AIP/0.12 TPAOH/60 H_2O/4 EtOH. For synthesizing CuO@Si-Beta zeolite (Si/Al = ∞) DSHSs, Si-Beta zeolite (Si/Al = ∞) nanocrystals were used and the secondary growth was performed at 170 °C for 15 h in a sol composed of 1 SiO_2/6.25 TEAOH/6.25 NH_4F/100 H_2O, using a rotating Teflon-lined stainless steel autoclave.

Ex situ characterization methods. The crystal phases were examined by XRD using a Bruker D2 Phaser (2nd Gen) instrument with a Co Kα radiation source (λ = 1.789 Å) or a Rigaku Ultima IV diffractometer with a Cu Kα radiation source (λ = 1.5406 Å). Raman spectra were acquired on a Renishaw inVia microscope using a ×50 objective (0.5 numerical aperture), 1,200 l/mm grating and a 532 nm diode laser excitation. The surface functional groups were analysed by Fourier Transform Infrared (FTIR) spectroscopy in transmission mode using a Perkin-Elmer 2000 instrument with a deuterated triglycine sulfate detector at a resolution of 4 cm^{-1}. The FTIR intensities of the samples were normalized to the same weight. Nitrogen physisorption was measured at liquid nitrogen temperature using a Micromeritics TriStar 3000 analyser. The zeta (ζ)-potentials of S-1 nanocrystals (1 wt% in H_2O), CSs (1 g l^{-1} in H_2O) and Fe^{3+}-CSs (1 g l^{-1} in H_2O) were measured at room temperature using a Malvern Zetasizer Nano-Z instrument. Scanning electron microscopy (SEM) images were taken on a Phenom GSR Desktop instrument operated at 10 eV or an XL-30 (Philips) instrument operated at 5 eV or a Helios NanoLab G3 UC (FEI) instrument operated at 5 kV. (Scanning) transmission electron microscopy ((S)TEM) images and energy-dispersive X-ray spectroscopy (EDS) results were recorded with an FEI Talos F200X transmission electron microscope, operated at 200 kV in bright field (TEM) or dark field (STEM) mode. The samples were found to be stable under the electron beam and no noticeable beam damage was observed. An ultramicrotomy technique was used to prepare the cross-sectional sample for TEM measurement, as recently reported by some of us[6].

The formed iron carbides were analysed using an MS-500 Mössbauer spectrometer (Oxford Instruments). The spectra were fitted with Lorentz lines using the least-squares method. The phase identification was based on the isomer shift, quadrupole splitting and hyperfine field strength of each Lorentzian line, which was calibrated relative to α-Fe. The pyridine-adsorbed infrared (IR) spectra were acquired on a Perkin-Elmer System 2000 instrument at a resolution of 4 cm^{-1}. The sample was pressed into a self-supported wafer and placed in an in situ IR cell. After pretreatment under vacuum ($p = 10^{-6}$ mbar) at 500 °C for 1 h, the sample was cooled to 150 °C, at which point a spectrum was acquired as background. The sample was further equilibrated with 0.1 mbar pyridine for 30 min followed by outgassing for 1 h, after which a spectrum of the sample with the chemisorbed pyridine was recorded. Temperature-programmed desorption (TPD) of NH_3 and C_3H_6 and H_2-temperature-programmed reduction (H_2-TPR) were performed on a Micromeritics AutoChemII 2920 instrument equipped with a thermal conductivity detector (TCD). Prior to each measurement, the sample was pretreated at 400 °C in He for 1 h. For NH_3-TPD, the adsorption of NH_3 was performed at 100 °C in He gas containing 10 vol% NH_3 for 1 h and TPD was performed in He flow by raising the temperature to 500 °C with a rate of 10 °C min^{-1}. For C_3H_6-TPD, the adsorption of gaseous C_3H_6 was performed at 50 °C for 1 h and TPD was performed in He by raising the temperature from 50 to 500 °C with a rate of 10 °C min^{-1}. For H_2-TPR, the reduction of the material was performed from 50 to 850 °C with a rate of 10 °C min^{-1} in a H_2–Ar mixture (5 vol% H_2). H_2 adsorption isotherms were acquired on a Micromeritics 3flex adsorption analyser. Prior to the adsorption test, the sample was first was placed in a vacuum at 150 °C for 12 h. H_2 adsorption isotherms were recorded using a RUBOTHERM magnetic suspension balance at 25 °C under increasing pressure from 0 to 20 bar.

In situ characterization methods. In situ Raman spectroscopy measurements were performed on a Renishaw inVia microscope coupled with a FTIR600 Linkam reactor, as illustrated in previous work[40]. Fe^{3+}-CSs loaded in the Linkam reactor were heated from room temperature to 500 °C with a ramping rate of 1 °C min^{-1} under static air, while Raman spectra were acquired using a ×50 objective (0.5 numerical aperture), 1,200 l/mm grating and a 532 nm diode laser excitation with an intensity of 0.32 mW (that is, 1.44×10^5 W cm^{-2}) with 4 acquisitions of 10 seconds. In situ XRD experiments were carried out on a Bruker D8 Advance X-ray diffractometer equipped with an Anton Paar XRK900 reaction chamber, using Co Kα (λ = 1.790 Å) radiation. The Fe^{3+}-CSs@S-1 colloidal particles (~40 mg) were heated to 540 °C with a ramping rate of 1 °C min^{-1} under O_2/N_2 (v/v = 1/4, 20 ml min^{-1}) gas flow. XRD measurements were conducted for 2θ ranging from 5 to 50°, with a step width of 0.049° and a counting time of 371 s per step.

Catalytic reactions. The syngas conversion was performed on a high-pressure fixed-bed reactor built by Xiamen HanDe Engineering Co. Before reaction, the catalyst (0.3 g) was loaded in a titanium reactor (inner diameter of 8 mm) and reduced under H_2 flow at 400 °C for 2 h. After cooling to 100 °C, syngas with a H_2/CO ratio of 2:1 was introduced into the reactor. The pressure and temperature were raised to 3 MPa and 300 °C, respectively. Products were analysed using an online gas chromatograph equipped with a TCD and two flame ionization detectors (FID). A TDX-01 packed column was connected to the TCD, while RT-Q-BOND-PLOT and HP-Pona capillary columns were connected to the FID detectors. The hydrocarbon selectivity without CO_2 was calculated on a molar carbon basis among products including hydrocarbons. Carbon balances were all higher than 95%. Due to the complexity of the C_{5+} fraction, errors in the determined percentages for the aromatics and linear and branched hydrocarbons are about ±5%. The catalytic performances of the prepared catalysts after 15 h of reaction were typically used for discussion. As for the reference catalysts, b-Fe_2O_3 was prepared by a typical precipitation method using $Fe(NO_3)_3$ as the precursor and calcination conditions of 500 °C for 1 h with a ramping rate of 1 °C min^{-1} in static air. hs-Fe_2O_3 (Supplementary Fig. 3) was prepared by direct calcination of Fe^{3+}-CSs at 500 °C for 1 h with a ramping rate of 1 °C min^{-1} in static air. hs-Fe_2O_3+ZSM-5 composite was made by direct mixing of the as-prepared hs-Fe_2O_3 and ZSM-5 (Supplementary Fig. 9) with a mass proportion of 1:9. Fe_2O_3/ZSM-5 with the same composition (1:9) was made by impregnating ZSM-5 (Supplementary Fig. 9) with a predetermined volume of aqueous $Fe(NO_3)_3$ solution (0.1 M), followed by calcination at 500 °C for 1 h in static air. Before the reaction, hs-Fe_2O_3/ZSM-5, Fe_2O_3/ZSM-5 and Fe_2O_3@ZSM-5 DSHSs were subject to an ion-exchange treatment with NH_4NO_3 aqueous solution (1.0 M, 70 °C) followed by calcination at 500 °C for 6 h in static air.

Data availability

The data supporting the findings of this study are available within the paper and its Supplementary Information files. Source data are provided with this paper.

References

37. Selvin, R., Hsu, H. L., Roselin, L. S. & Bououdina, M. Effect of aging on the precursor sol for the synthesis of nanocrystalline ZSM-5. *Synth. React. Inorg. Met. Org. Nano. Met. Chem.* **41**, 1028–1032 (2011).
38. Roselin, L. S., Selvin, R. & Bououdina, M. Nanocrystalline ZSM-5: an efficient catalyst for regioselective acetolysis of epichlorohydrin. *Chem. Eng. Commun.* **199**, 221–230 (2012).
39. Yordanov, I. et al. Elucidation of Pt clusters in the micropores of zeolite nanoparticles assembled in thin films. *J. Phys. Chem. C* **114**, 20974–20982 (2010).
40. Hartman, T., Geitenbeek, R. G., Whiting, G. T. & Weckhuysen, B. M. Operando monitoring of temperature and active species at the single catalyst particle level. *Nat. Catal.* **2**, 986–996 (2019).

Acknowledgements

B.M.W. acknowledges financial support from the Netherlands Organization for Scientific Research (NWO) in the frame of a Gravitation Program MCEC (Netherlands Center for Multiscale Catalytic Energy Conversion, www.mcec-researchcenter.nl). X.X. (Utrecht University) acknowledges financial support from the EU H2020-MSCA-ITN-2015 project 'MULTIMAT' (project no. 676045). K.C. and Y.W. acknowledge financial support from the National Natural Science Foundation of China (grant nos. 91945301, 22121001 and 22072120). J.X. thanks D. Wezendonk (Utrecht University) for his help with the in situ XRD measurements.

Author contributions

J.X., B.M.W., K.C. and Y.W. conceived and designed the experiments. B.M.W. and Y.W. supervised the project. J.X. synthesized and characterized the materials, analysed the data and wrote the initial manuscript. K.C. and M.W. performed the catalytic reactions, analysed the resulting data and drafted the catalytic reaction part. X.X. and M.A.v.H. performed the (S)TEM-related measurements. Y.L. and T.H. performed the ex situ IR and in situ Raman measurements, respectively. S.X. performed a part of the SEM measurements and the ex situ Raman measurements. D.F. and K.B. contributed to the exploration of the zeolite secondary growth conditions. A.v.B. helped with the mechanistic understanding of the self-assembly process. J.X., B.M.W., K.C. and Y.W. revised the paper with contributions from all the other co-authors.

Competing interests

The authors declare no competing interests.

Additional information

Supplementary information The online version contains supplementary material available at https://doi.org/10.1038/s41563-021-01183-0.

Correspondence and requests for materials should be addressed to Ye Wang or Bert M. Weckhuysen.

Peer review information *Nature Materials* thanks Michael Claeys and the other, anonymous, reviewer(s) for their contribution to the peer review of this work.